CHEMISTRY OF MATERIALS

Article

pubs.acs.org/cm

Investigating the Energy Storage Mechanism of SnS_2-rGO Composite Anode for Advanced Na-Ion Batteries

Chuze Ma,[†] Jing Xu,[†,§] Judith Alvarado,[†] Baihua Qu,[‡] James Somerville,[†,∥] Jim Yang Lee,[‡] and Ying Shirley Meng*[,†]

[†]Department of NanoEngineering, University of California San Diego, 9500 Gilman Drive, La Jolla, California 92037, United States

[‡]Department of Chemical and Biomolecular Engineering, National University of Singapore, 10 Kent Ridge Crescent, 119260 Singapore, Singapore

Supporting Information

ABSTRACT: Tin sulfide–reduced graphene oxide (SnS_2-rGO) composite material is investigated as an advanced anode material for Na-ion batteries. It can deliver a reversible capacity of 630 mAh g^{-1} with negligible capacity loss and exhibits superb rate performance. Here, the energy storage mechanism of this SnS_2-rGO anode and the critical mechanistic role of rGO will be revealed in detail. A synergistic mechanism involving conversion and alloying reactions is proposed based on our synchrotron X-ray diffraction (SXRD) and *in situ* X-ray absorption spectroscopy (XAS) results. Contrary to what has been proposed in the literature, we determined that Na_2S_2 forms instead of Na_2S at the fully discharge state. The as-formed Na_2S_2 works as a matrix to relieve the strain from the huge volume expansion of the Na–Sn alloy reaction, shown in the high resolution transmission electron microscope (HRTEM). In addition, the Raman spectra results suggest that the rGO not only assists the material to have better electrochemical performance by preventing particle agglomeration of the active material but also coordinates with Na-ions through electrostatic interaction during the first cycle. The unique reaction mechanism in SnS_2-rGO offers a well-balanced approach for sodium storage to deliver high capacity, long-cycle life, and superior rate capability.

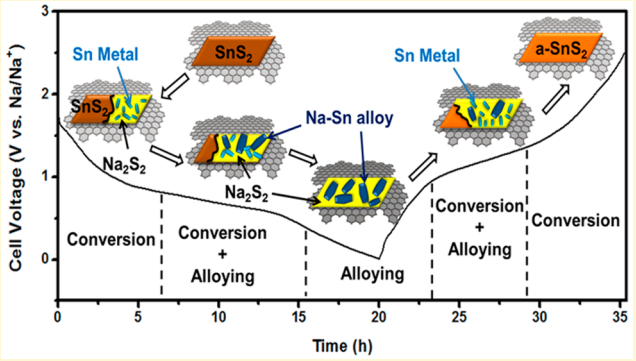

1. INTRODUCTION

The pressing demand for economically accessible and environmentally benign energy storage technologies has strongly promoted the need for scientific study in this area. Alternative energy storage systems for lithium-ion technology are drawing more attention in the field of rechargeable batteries.[1,2] The large abundance of Na, low cost, and suitable redox potential of rechargeable Na-ion batteries (NIBs) show great promise for energy storage applications.[2] Research on NIBs can be traced back to the 1970s, when Delmas et al. began to study the structure properties of Na_xTMO_2.[3,4] The major obstacle in realizing NIBs in practice was the absence of suitable negative electrodes. On the other hand, the research and commercialization of lithium-ion batteries (LIBs) gained huge success due to the discovery of the graphite anode in the 1990s.[5] As a result, limited efforts were devoted to NIBs in the last two decades.

Because the demand for large-scale batteries for electric energy storage systems increased, the research interest in NIBs was revitalized in 2010. Although several breakthroughs were made on cathodes for NIBs, the anode remains as the main bottleneck.[6−8] Graphite gained massive attention because of LIBs; however, Na ions are not able to intercalate unless diglyme-based electrolyte are used by adopting a cointercalation mechanism.[9] Therefore, several nongraphitic carbon anodes have been studied.[10] Tin and tin-based compounds have drawn much attention as high-capacity NIB anodes because of the theoretical stoichiometry of $Na_{15}Sn_4$ (847 mAh g^{-1}) and low redox potential.[11] Various Sn-based materials were explored as potential high energy anodes for NIBs.[12−21] For instance, Komaba et al. demonstrated that Sn powder electrodes with polyacrylate binder delivers a capacity of 500 mAh g^{-1} in aprotic Na cells for 20 cycles.[12] Sn-SnS-C nanocomposites have demonstrated reversible capacities of 664 mAh g^{-1} at 20 mA g^{-1} and 350 mAh g^{-1} at 800 mA g^{-1}.[19] Kim and co-workers reported the use of Sn_4P_3 as a promising anode material, which delivers a reversible capacity of 718 mAh g^{-1} with stable cycle performance.[20] Very recently, we proposed a novel SnS_2-rGO composite anode with excellent electrochemical performance for NIBs.[22] The SnS_2-rGO electrode demonstrated a high reversible capacity (630 mAh g^{-1} at 0.2 A g^{-1}), good rate performance (544 mAh g^{-1} at 2 A g^{-1}), and long cycle-life (500 mAh g^{-1} at 1 A g^{-1} for 400 cycles). In this material, intuitively, the SnS_2 should first undergo a conversion reaction with Na to form Sn and Na_2S. Then Sn should further

Received: May 27, 2015
Revised: July 11, 2015
Published: July 21, 2015

DOI: 10.1021/acs.chemmater.5b01984
Chem. Mater. 2015, 27, 5633−5640

alloy with Na to form the $Na_{15}Sn_4$ alloy phase. However, a more in-depth study of the SnS_2-rGO composite reveals a sophisticated reaction pathway.

A comprehensive study on the energy storage mechanism of the SnS_2-rGO composite as the anode material in NIBs is reported. The structural evolution and phase transformation of the electrode upon discharge/charge are tracked by synchrotron X-ray diffraction (SXRD) and high-resolution transmission electron microscopy (HRTEM). It is found that Sn appears as an intermediate product which then turns into $Na_{15}Sn_4$ alloy during sodiation. Moreover, Na_2S_2 is confirmed as the final reaction product rather than Na_2S. The SnS_2 becomes amorphous upon insertion/removal of Na-ions after a full cycle. Meanwhile, in situ X-ray absorption spectroscopy (XAS) was utilized to elucidate the local structure evolution and reveal the detailed sodiation mechanism. We observed a synergistic mechanism which reveals the occurrence of simultaneous conversion and alloy reactions. The importance of this unique mechanism is discussed in terms of reaction kinetics and cycling performance. In order to determine the contribution of rGO in the electrochemical performance, the charged/discharged samples were characterized by Raman spectroscopy. Here, rGO prevents particle agglomeration during the formation of SnS_2, which will be explained in further detail. These studies enable us to understand the underlying principles that allow SnS_2-rGO to achieve excellent electrochemical performance, therefore, providing guidelines to design advanced anode materials for high-energy NIBs.

2. EXPERIMENTAL SECTION

2.1. Material Synthesis and Characterization. The materials were synthesized following previous published work.[22] Graphite oxide (GO) was prepared from graphite powder by a modified Hummers' method.[23] The typical synthesis of the SnS_2-rGO composite is as follows: 0.7015 g of $SnCl_4{\cdot}5H_2O$ (Alfa Aesar) and 0.6014 g of thioacetamide (TAA) (Sigma-Aldrich) were added to 40 mL of 1.5 mg mL^{-1} GO suspension under stirring. The mixture was sonicated for 30 min before transferring it to a 50 mL Teflon-lined stainless steel autoclave and heated at 160 °C for 12 h. After cooling to room temperature, the solid product was centrifuged, washed with deionized water and absolute alcohol (three times each), and then vacuum-dried at 60 °C overnight. Pure SnS_2 was synthesized under the same conditions but without the presence of GO. The dried product was then heated in Ar at the rate of 5 °C $minutes^{-1}$ to 400 °C and maintained for 4 h. The material was characterized by a Philips XL30 environmental scanning electron microscope (ESEM) operating at 10 kV and an FEI Tecnai G2 Sphera transmission electron microscopy (TEM) operating at 200 kV. Powder X-ray diffractions (XRD) were recorded on a Bruker pXRD using Cu Kα radiation.

2.2. Synchrotron X-ray Diffraction (SXRD). The samples characterized by XRD were obtained by disassembling the cycled batteries in an argon filled glovebox. The electrode materials were washed using battery grade dimethyl carbonate (DMC) three times and then stripped off from the aluminum current collectors. The powders from the cycled electrode were then mounted in the hermitically sealed capillary tubes for ex situ XRD. Powder diffractions of all samples were taken using synchrotron XRD at the Advanced Photon Source (APS) on beamline 11-BM (l = 0.459 Å). The beamline uses a sagittal focused X-ray beam with a high precision diffractometer circle and perfect Si (111) crystal analyzer detection for high sensitivity and resolution. XRD patterns were collected between 0.3° and 50.0° in 2θ angles.

2.3. In Situ X-ray Absorption Spectroscopy (XAS). X-ray absorption spectroscopy measurements were performed at 20-BM-B beamline of Applied Photon Source (APS) at Argonne National Laboratory. Customized coin cells were used to prevent the sample contamination. Measurements at the Sn K-edge were performed under transmission mode using a gas ionization chamber to monitor the incident and transmitted X-ray intensities. A third ionization chamber was used in conjunction with a Sn-foil standard to provide internal calibration for the alignment of the edge positions. The incident beam was monochromatized using a Si (111) double-crystal fixed exit monochromator. Harmonic rejection was accomplished using a rhodium-coated mirror. Each spectrum was normalized using the data processing software package IFEFFIT.[24]

2.4. Raman Spectroscopy. The cycled electrodes were washed with battery grade DMC to remove any residual salt. In an argon filled glovebox, the electrodes were placed in a customized Raman sample holder to prevent air exposure during the analysis. Using a Renishaw inVia Raman Microscope, the samples were exposed to a green laser (532 nm wavelength) with a spot size of 5 μm in diameter for 20 s at one acquisition. The laser intensity was 10% in order to minimize sample damage. All of the samples were taken from 250 to 2000 cm^{-1} spectra range and with a 40× objective lens.

2.5. Electrochemical Tests. Electrodes were prepared from slurries containing 80 wt % of active material (based on the total mass of the SnS_2-rGO composite), 10 wt % of Na-alginate as a binder, and 10 wt % Super P carbon black as a carbon additive in deionized water. The slurries were then cast on aluminum foil and dried in vacuum at 80 °C. Typical loading of the active material was 2 mg cm^{-2}. A glass fiber GF/F (Whatman) filter was used as the separator, and 1 M $NaPF_6$ in a 1:1 (v/v) mixture of ethylene carbonate (EC) and diethyl carbonate (DEC) was used as the electrolyte. Battery assembly was carried out in an MBraun glovebox (H_2O < 0.1 ppm). Galvanostatic discharge and charge at various current densities were performed on an Arbin BT2000 battery cycler.

3. RESULTS AND DISCUSSION

3.1. Electrochemical Performances of SnS_2-rGO. Figure 1 (a) shows the galvanostatic charge−discharge voltage profiles

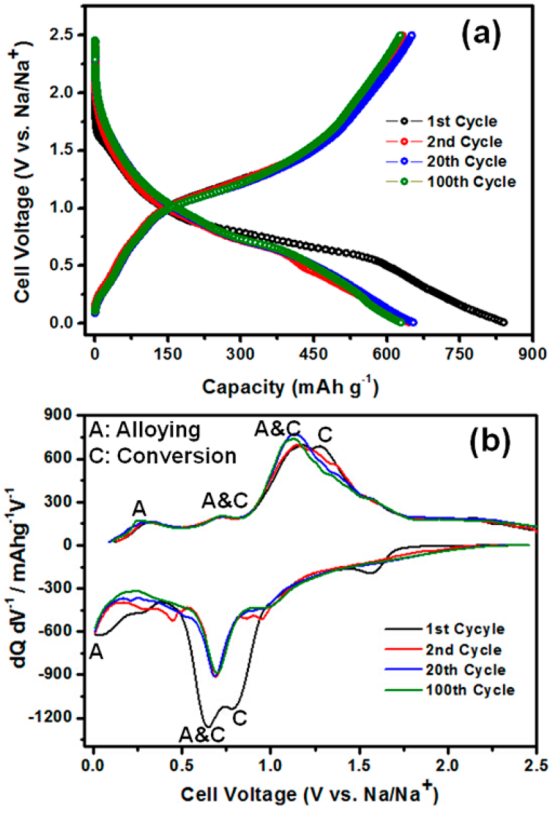

Figure 1. (a) Voltage profiles and (b) dQ dV^{-1} plots of the SnS_2-rGO composite material.

DOI: 10.1021/acs.chemmater.5b01984
Chem. Mater. 2015, 27, 5633−5640

of the SnS_2-rGO composite electrode at the current density of 0.2 A g^{-1} at the 1st, 2nd, 20th, and 100th cycles. In the first cycle, the material exhibited a reversible capacity of 630 mAh g^{-1} with 75% Coulombic efficiency. After 100 cycles, the anode maintained a capacity of 627 mAh g^{-1}, exhibiting excellent capacity retention. In our previous work, this material demonstrated superb performance at high current density, which is shown in Figure S3.[22] Although the voltage profiles look smooth without any voltage plateaus, the corresponding dQ dV^{-1} curves for each cycle plotted in Figure 1 (b) indicate that multiple reactions occur during electrochemical cycling. In the first cycle, a reduction peak around 1.7 V is assigned to the intercalation of the Na-ions into SnS_2 (0 0 1) plane.[25] The major reduction peaks around 0.7 V are due to the combination of the synergetic conversion and alloying reactions as well as the irreversible formation of the solid electrolyte interphase (SEI). The peaks around 0.3 and 0.01 V could be ascribed to the formation of Na−Sn and Na−S phases. During the charge state, the oxidation peaks around 0.3 and 0.7 V originate from the desodiation of Na−Sn and Na−S phases. The broad peak from 1.0 to 1.5 V is attributed to the desodiation of the Na−Sn alloy phases and the reformation of SnS_2. The peaks in the dQ dV^{-1} curves overlap over subsequent cycles, indicating good stability and reversibility after the first cycle.

3.2. Structure Evolution Characterized by SXRD and In Situ XAS. To obtain direct evidence of the phase transformations during electrochemical cycling, we carried out ex situ SXRD analysis on the SnS_2-rGO electrode at different discharge and charge states. The XRD pattern at the pristine state confirmed the crystallinity of the as-synthesized SnS_2 and was indexed as trigonal space group *P*3*m*1 (Figure S1). As shown in Figure 2, the diffraction peaks of the SnS_2 phase

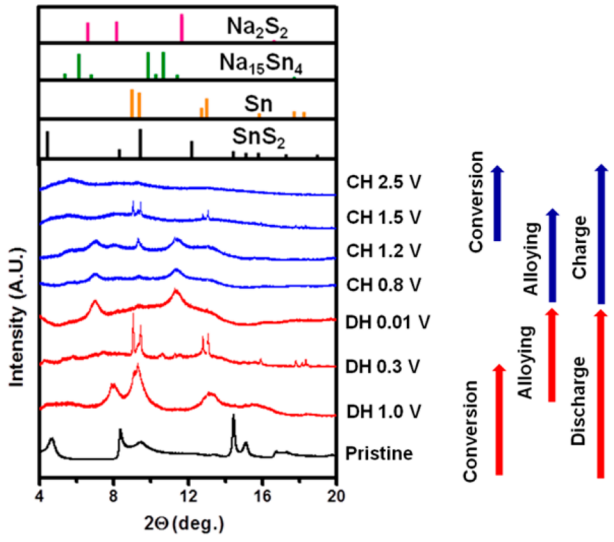

Figure 2. Synchrotron X-ray diffraction results of SnS_2-rGO electrodes at different discharge/charge states.

gradually disappear during the discharge state, while two broad peaks around 9.1° and 13.2° appear, indicating the formation of the Sn phase.

At 0.3 V, the XRD patterns of the discharged electrode matched well with the diffraction patterns of Sn. By applying the Scherrer Equation to the two most intense XRD peaks, the Sn particle size is less than 3 nm.[26] After further discharge, the Sn diffraction peaks disappeared, accompanied by the appearance of two new broad peaks around 7.0° and 11.5°. The newly observed peaks resulted from the Na_2S_2 phase. From these observations, it clearly demonstrates that nanosized Sn particles first nucleate from the conversion reaction of Na and SnS_2. Later, the increasing quantity of Na in the Sn host structure results in the formation of amorphous Na−Sn alloys through a series of phase transitions, thus the crystalline Sn diffraction peaks disappeared.[13,14] In the Li-ion system, it is widely acknowledged SnS_2 reacts with Li-ions to form Li_2S. Therefore, previous publications assumed that Sn−S compounds react with Na-ions to produce Na_2S.[19,27] However, the observation of the Na_2S_2 phase in this work is intrinsically different, as it could originate from the differences between Li−S and Na−S alloys.[28] After charging the electrode to 1.2 V, the Sn diffraction peaks began to appear and dominate at 1.5 V. This is the result of the dealloying reaction from the Na−Sn alloy. Simultaneously, the XRD peaks of the Na_2S_2 phase dwindled until it disappeared. When the electrode was charged to 2.5 V, there were no well-defined XRD peaks detected. This suggests that the Sn converted to a phase with low crystallinity or to an amorphous state, presumably SnS_2. It is interesting to note that the appearance/disappearance of Na_2S_2 occurred along with the Na−Sn alloying reaction, indicating that the conversion and alloying reactions happen simultaneously in the lower voltage region. This synergistic effect can accelerate the kinetics of the reactions and improve the structure stability of the material.[29] In situ X-ray absorption spectroscopy (XAS) was performed at the Sn K-edge for the active electrode material to reveal more time-resolved information and track the evolution of local structures.

Figure 3 represents Fourier transforms of the selected Sn K-edge EXAFS patterns as a function of cell voltage. The peaks

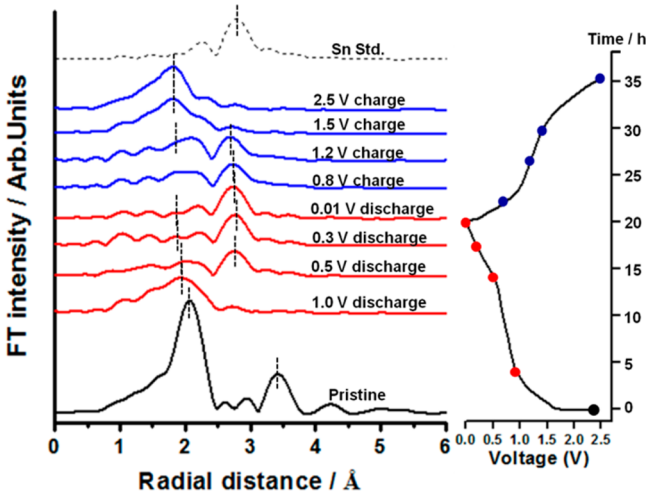

Figure 3. Sn K-edge EXAFS spectra of SnS_2-rGO electrodes at different voltages in the first cycle.

around 1.9 and 3.4 Å in the pristine sample are related to the Sn−S and Sn−Sn interactions, respectively. As the electrode was discharged, the intensity of both peaks decreased significantly due to the displacement of reactive species during the conversion reaction. Meanwhile, a peak around 2.77 Å began to appear and continued to grow upon discharge, belonging to the Sn−Sn interaction in the phase of Sn that nucleated from the conversion reaction.[30,31] The Sn−S peak was observed until the final discharge state, showing the

DOI: 10.1021/acs.chemmater.5b01984
Chem. Mater. 2015, 27, 5633−5640

depletion of SnS_2. The formation of Na−Sn alloy phases are determined by the decrease in the interatomic distance of the Sn−Sn shell from 2.77 to 2.74 Å at the fully discharged state.[31] Given the amorphous feature of Na−Sn phases and their similar Sn−Sn bond length to the Sn metal, it is hard to determine the exact voltage at which they begin to form. However, previous reports claim that Na−Sn alloy reactions occur starting at 0.7 V.[11,13] Therefore, we propose that the Sn metal generated from the conversion reaction alloys with Na-ions before all the SnS_2 is converted. This is regarded as a synergistic mechanism since it takes advantage of both the conversion and the alloying reactions. The fast kinetics pertaining to the alloying reactions reduces the cell polarization, and the Na_2S_2 matrix formed in the conversion reaction helps to accommodate the huge volume variations of Na−Sn alloys. During the first charge, consistent with XRD result, the Sn−S peaks appeared accompanied by the disappearance of the Sn−Sn peaks. At 1.2 V, we observed both the Sn−S interaction from SnS_2 and the Sn−Sn interaction in the Na−Sn alloy phases, which indicates that the SnS_2 phase was being reconstructed at this voltage. Comparing the XAS results to the XRD results (Figure 2) at 1.2 V, the Na−Sn dealloying reactions were occurring as the SnS_2 were forming; therefore, the alloying and conversion reactions occurred simultaneously again during the charge. The Sn−S peak of the fully charged sample has a smaller interatomic distance and intensity compared to the peak of the pristine SnS_2-rGO sample. Meanwhile, the Sn−Sn interaction of the pristine sample did not regenerate at the fully charged state, demonstrating the formation of nanoclustered SnS_2 rather than the crystalline SnS_2 phase (as in the pristine state).[20] Both of the EXAFS and XRD observations portray that the long-range ordering decreases as Na ions are inserted in the SnS_2 structure, due to the transformation from crystalline to amorphous found in the active material. After all, the in situ XAS provides more evidence for the synergistic reaction mechanism for SnS_2.

3.3. TEM Studies of the Cycled Materials. In order to further confirm the proposed reaction mechanism, the cycled electrodes were characterized by HRTEM to obtain a direct image of the structure. Figure 4 (a) shows the SnS_2-rGO electrode after the first discharge where the nanoparticles (~10 nm) were embedded in an amorphous matrix. The nanoparticles are Na−Sn alloys that originated from the nanocrystalline Sn formed during the conversion reaction. Comparing the size of the Na−Sn alloy to the Sn metal (~3 nm), the volume of the nanoparticles expands by more than 300%. Therefore, the amorphous Na_2S_2 matrix surrounding the nanoparticles relieves the strain from volume expansion. The coexistence of amorphous Na_2S_2 and $Na_{15}Sn_4$ phases are also identified by selected area electron diffraction (SAED) (Figure 4 (b)). The diffusive rings from the Na_2S_2 diffraction is more pronounced because it occupies the major space of the selected area, while the diffraction patterns from the $Na_{15}Sn_4$ phase are relatively faint. Figure 4 (c) shows the TEM images from another area in the discharged electrode material. Here the lattice fringes could be observed from the nanoparticles because they were on the surface or the edge of the amorphous matrix. The SAED diffraction patterns show the existence of the $Na_{15}Sn_4$ phase with amorphous features. It is difficult to identify the $Na_{15}Sn_4$ phase by solely relying on the XRD patterns because of the lack of long-range ordering and particle distribution within the Na_2S_2 and rGO matrix. Therefore, the HRTEM and SAED provided more information about samples

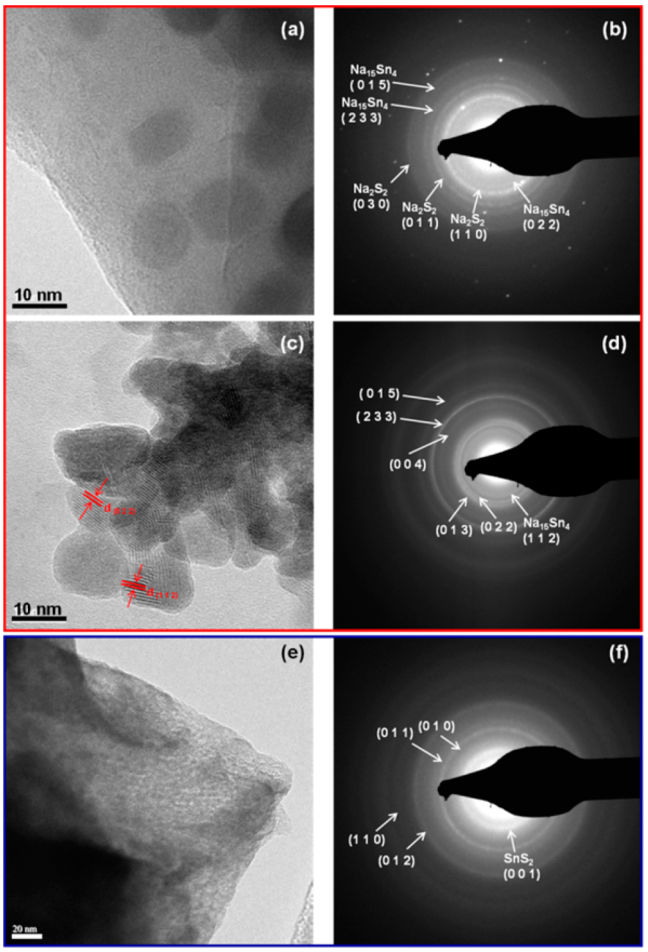

Figure 4. TEM and SAED results for (a)-(d) the SnS_2-rGO electrode after first discharge and (e),(f) the SnS_2-rGO electrode after first charge.

after sodiation. The TEM image of the electrode material at the fully charged state is present in Figure 4 (e). Here, the material became completely amorphous, and no clear grain boundaries were observed within the particle. Correspondingly, the SAED result demonstrates that the amorphous SnS_2 phase forms at the charged state, which is also consistent with our XRD and XAS studies mentioned above.

Based on the characterizations thus far and considering the amount of Na storage capacity according to the electrochemical results, the overall reaction equation could be written as follows:

$$SnS_2 + 2Na^+ + 2e^- \rightleftarrows Sn + Na_2S_2 \quad \text{(theoretical capacity: 293 mAh g}^{-1}\text{)} \tag{1}$$

$$Sn + 3.75Na^+ + 3.75e^- \rightleftarrows Na_{3.75}Sn \quad \text{(theoretical capacity: 549 mAh g}^{-1}\text{)} \tag{2}$$

The overall theoretical capacity for SnS_2 is 842 mAh g^{-1}. Considering there is 12% rGO in the composite material which delivers negligible reversible capacity,[22] the theoretical capacity for SnS_2-rGO is 740 mAh g^{-1}.

3.4. Study the Composite Material by Raman Spectra. Raman spectroscopy was used to characterize the pristine and cycled electrodes in order to determine the properties of rGO and SnS_2 (Figure 5). As previously stated, the 2H-SnS_2

DOI: 10.1021/acs.chemmater.5b01984
Chem. Mater. 2015, 27, 5633−5640

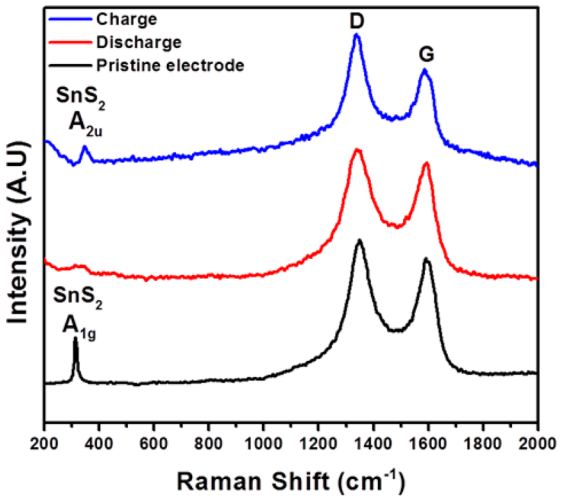

Figure 5. Raman spectra of the SnS_2-rGO electrode at the pristine state (black), after first discharge (red), and after first charge (blue).

Table 1. Raman Vibration Modes of Peaks Found in Figure 5

sample	vibration mode	SnS_2 (cm^{-1})	rGO (cm^{-1})	I_D/I_G
pristine electrode	D		1350.3	1.2
	G		1594.1	
	A_{1g}	314.8		
discharge 0.01 V	D		1343.2	1.02
	G		1594.1	
charge 2.5 V	D		1351.6	1.3
	G		1598.1	
	A_{2u}	361.1		

Table 2. Raman Vibration Modes for SnS_2 Found in Figure 6

sample	spot	vibration mode	SnS_2 (cm^{-1})
		E_g	179.0
discharge 0.01 V	1−3	A_{2u}	348.5
charge 2.5 V	1	A_{2u}	349.8
		E_g	175.7
	2	A_{2u}	345.5
		E_u	221.2
		E_g	175.7
	3		

nanoparticles used in this study correspond to the D^3_{3d}-$P3m1$ space group. The crystal structure contains three atoms per unit cell extending in a sandwich layer.

The irreducible representations of the D_{3d} point group are found at the center of the Brillouin zone, Γ:

$$\Gamma = A_{1g} + E_g + 2A_{2u} + 2E_u$$

These optic modes can be divided into three Raman-active modes (A_{1g}, E_g) and three infrared-active modes (A_{2u}, E_u).[32,33]

In black, the pristine electrode exhibits a sharp peak at 314.8 cm^{-1} which corresponds to the A_{1g} Raman active vibration mode.[25,32−36] Meanwhile, the rGO is characterized by the graphitic G band located at 1594.1 cm^{-1}, which is related to the vibration of the sp^2-bonded carbon atoms in a two-dimensional lattice (Table 1). The disorder and defects in the hexagonal graphitic layer correspond to the D band at 1350.3 cm^{-1}.[22,35,37,38] As shown in our previous work, the intensity ratio of the D band to the G band (I_D/I_G) was calculated as 1.2 (Table 1), which resulted from the decreased sp^2 domains and unrepaired defects during the reduction of GO.[35] The electrode discharged to 0.01 V (in red) shows the elimination of the A_{1g}

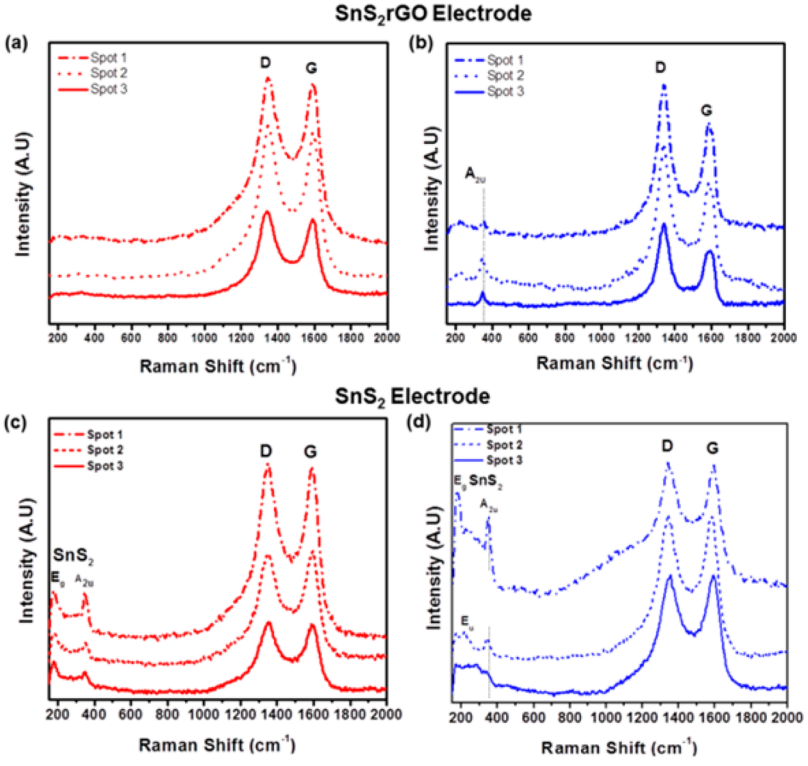

Figure 6. Raman spectra on different spots of SnS_2 electrodes with and without rGO. (a) SnS_2-rGO electrode at fully discharge. (b) SnS_2-rGO electrode at fully charge. (c) Bare SnS_2 electrode at fully discharge. (d) Bare SnS_2 electrode at fully charge.

DOI: 10.1021/acs.chemmater.5b01984
Chem. Mater. 2015, 27, 5633−5640

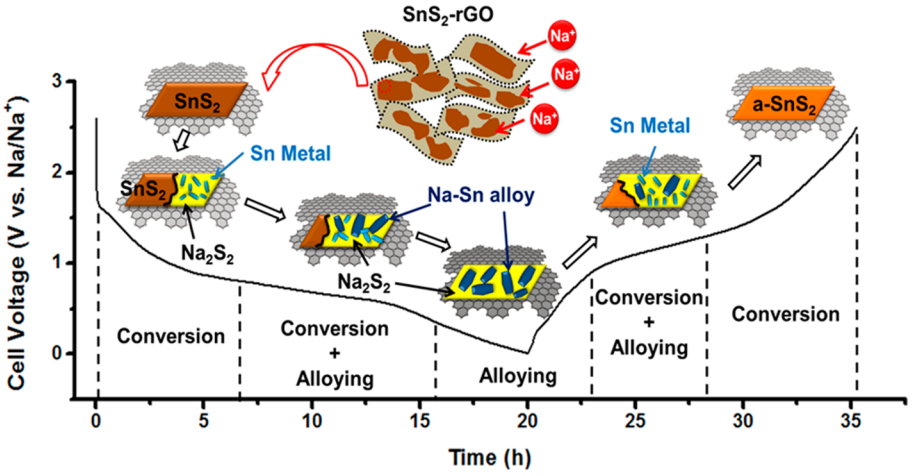

Figure 7. Schematic of the energy storage mechanism of the SnS_2-rGO composite.

peak for SnS_2 Raman vibration mode, which demonstrates the full consumption of SnS_2. Moreover, the I_D/I_G ratio drops to 1.02, suggesting that rGO is involved during the sodiation process. The change in intensity ratio (I_D/I_G) is an indication that the rGO sheets order themselves through an electrostatic interaction, which can occur between the rGO sheets and Na-ions.[38] Once the electrode is fully charged to 2.5 V (blue), the I_D/I_G ratio of the rGO sheets returns to 1.3, close to the pristine state. This is an indication that Na-ion could reversibly insert/remove from the rGO, presumably due to the increased distance of the carbon layers. The intensity ratios and peak positions are summarized in Table 1. The appearance of the A_{2u} peak in the Raman spectrum (blue) for the fully charged electrode suggests the good reversibility of SnS_2. However, we observed a red shift in the broad A_{2u} infrared vibration mode, which is attributed to the formation of nanoparticles and is in agreement with the above-mentioned results.[33]

3.5. The Effect of rGO. Not only does the rGO play a role in accommodating the Na_2S_2 alloy, but it also allows for the pristine SnS_2 to be fully consumed and prevents particle agglomeration. Figure 6 shows the Raman spectra taken for each electrode at three different spots. This was done to ensure proper reproducibility within the electrode, given that the Raman has a spot size of 5 μm in diameter. For the SnS_2-rGO electrode, all three spots exhibit the disappearance of the A_{1g} peak at the fully discharge state and the occurrence of the A_{2u} peak at the charge state (Figure 6 a and b). This proves that the SnS_2 is fully consumed in discharge and reformed in the charge state, as discussed in Figure 5. In contrast, the bare SnS_2 electrode showed varied results among different spots. In Figure 6 (c), the A_{2u} and E_g peaks from the SnS_2 phase were present after the electrode was discharged to 0.01 V, demonstrating that not all of the SnS_2 is consumed in the bare SnS_2 electrode. At the fully charge state, the Raman spectrum of each spot within Figure 6 (d) is significantly different, indicating that SnS_2 is not regenerated uniformly throughout the electrode. For instance, spot 3 shows that there is no Raman vibration mode for SnS_2 nanoparticles, while spot 1 displays a strong A_{2u} peak. These variations within the Raman results at different spot positions indicate that the formation of SnS_2 in the bare SnS_2 electrode is not fully reversible or uniformly distributed. Therefore, some SnS_2 particle agglomeration occurred during the charge process. Clearly the rGO plays a critical role in evenly dispersing the SnS_2 particles during electrochemical cycling. The rGO allows for a thorough depletion of SnS_2 at the fully discharged state and prevents particle agglomeration during the charged state, thus facilitating the reversibility in reactions (see Table 2).

3.6. Energy Storage Mechanism of SnS_2-rGO. The proposed energy storage mechanism according to the systematic characterizations above is summarized in Figure 7.

During the discharge, the conversion reaction between SnS_2 and Na-ions is the major reaction that occurs above 0.8 V, which generates Sn nanoparticles and amorphous Na_2S_2. Before all the SnS_2 is consumed, the alloy reactions between the Sn metal and Na-ions begin, leading to Na−Sn alloy phases. Therefore, during this region the conversion and alloying reactions happen simultaneously, denoted as the 'conversion + alloying' region. Upon further discharging, the alloying reactions become more dominant below 0.3 V. At the final state of discharge, the nanosized $Na_{15}Sn_4$ and Na_2S_2 matrix are the final reaction products. The specific capacity calculated based on this reaction is 842 mAh g^{-1} for SnS_2 and 740 mAh g^{-1} for SnS_2-rGO, which correlates well with our electrochemical results. During the charge, the whole reactions are reversed so that the $Na_{15}Sn_4$ first dealloys and reforms the Sn metal. Then the Sn metal further reacts with Na_2S_2 to reconstruct the SnS_2 phase. Once again, the alloying and conversion reactions happen concurrently between 1.0 to 1.5 V. With all the Na−Sn alloy phases transferring to Sn, the conversion reaction becomes the major reaction again, similar to the beginning of discharge. However, the SnS_2 phase that formed at the final state of charge is no longer crystalline and becomes amorphous. The Raman spectra results suggest that the rGO also reacts reversibly with the Na-ions during this process, reflected by the reversible carbon D band and G band intensity ratio change. Although the detailed rGO mechanism is yet to be determined and the electrochemical data for rGO cycled in half cell shows insignificant reversible capacity, we believe that it is still a very interesting phenomenon. This result may inspire us to conduct further research on graphite based anode material for NIBs. Meanwhile, it is clearly demonstrated that rGO largely prevents particle agglomeration during electrochemical cycling, which helps with a complete and uniform consumption of SnS_2. Overall, the excellent electrochemical performance of the composite material should be mainly attributed to the synergistic mechanism of SnS_2, since it is the major active material for Na-ions storage. The fast

DOI: 10.1021/acs.chemmater.5b01984
Chem. Mater. 2015, 27, 5633−5640

kinetics of the alloy reactions solves the long-term criticized problem of high voltage hysteresis and poor rate performance from conversion reaction. In return, better cycling performance can be achieved with the Na_2S_2 matrix, which solves the volume expansion problem caused by the alloying reactions. With the assistance of rGO, the unique conversion-alloying mechanism in SnS_2-rGO offers a well-balanced approach for sodium storage to deliver high capacity, long-cycle life, and superior rate capability. We believe that the nanocomposite materials design principles from this study can also be applied to other systems that involve both conversion and alloy reactions, such as SnO, Sb_2O_3, or SnS.

4. CONCLUSION

An in-depth understanding of the underlying relation between Na insertion/extraction mechanisms and electrochemical performances is essential to improve the performances of Na-ion batteries. In this work, a novel Na anode material, SnS_2-rGO, has been comprehensively investigated using SXRD, XAS, TEM, and Raman spectroscopy. The material demonstrates a capacity of 630 mAh g^{-1} with excellent capacity retention and rate performance. Contrary to what has been proposed in the literature, Na_2S_2 instead of Na_2S forms during the synergistic reaction, as confirmed by the XRD and SAED results. The interatomic distance change of the Sn−Sn interaction in the EXAFS results indicates that Na−Sn alloy phases form during the discharge, while the SAED observations identify the alloy phase to be amorphous $Na_{15}Sn_4$. Highly amorphous SnS_2 forms after one full cycle, presumably due to the breakdown of pristine SnS_2 into Sn nanoparticles during the discharge. The synergistic mechanism that takes advantages of both conversion and alloying reactions ensures the high specific capacity, long cycle life, and fast kinetics. The rGO allows for effective dispersion of the pristine SnS_2 particles and prevents the agglomeration of the nanosized reaction products. Besides serving as a matrix to mitigate the mechanical strain, the rGO also reversibly reacts with Na-ion in the first cycle. Benefiting from both the synergistic effect and the assistance of rGO, highly efficient and durable sodium storage is achieved by this SnS_2-rGO anode in NIBs.

■ ASSOCIATED CONTENT

Supporting Information

The Supporting Information is available free of charge on the ACS Publications website at DOI: 10.1021/acs.chemmater.5b01984.

XRD for SnS_2-rGO, SEM, and EDX for SnS_2-rGO; voltage profiles, cycling properties, and rate performance of SnS_2-rGO and SnS_2; SEM images of electrodes before and after cycling (PDF)

■ AUTHOR INFORMATION

Corresponding Author

*E-mail: shmeng@ucsd.edu.

Present Addresses

[§]Environmental Energy Technologies Division, Lawrence Berkeley National Laboratory, Berkeley, CA 94720, USA.

[∥]Linacre College, St. Cross Road, Oxford OX1 3JA, UK.

Author Contributions

The manuscript was written through contributions of all authors. All authors have given approval to the final version of the manuscript.

Funding

C.M., J. X., and Y.S.M. are grateful for the financial support from the USA National Science Foundation under Award Number 1057170. J.A. acknowledges the AGEP GSR fellowship, which is the supplement fund to the DMR1057170. Prof. J. Y. Lee and Dr. B. H. Qu would like to acknowledge the financial support from A*STAR Project 1220203049 (R279-000-370-305) and the International Science and Technology Cooperation Program of China (2012DFG42100).

Notes

The authors declare no competing financial interest.

■ ACKNOWLEDGMENTS

The ex situ synchrotron X-ray diffraction patterns were collected at Argonne National Laboratory on beamline 11-BM. The authors appreciate the fruitful discussion and assistance from Dr. Mahalingam Balasubramanian at beamline 20-BM-B of Argonne National Laboratory.

■ REFERENCES

(1) Kim, S. W.; Seo, D. H.; Ma, X.; Ceder, G.; Kang, K. Electrode Materials for Rechargeable Sodium-Ion Batteries: Potential Alternatives to Current Lithium-Ion Batteries. *Adv. Energy Mater.* **2012**, *2*, 710−721.

(2) Ellis, B. L.; Nazar, L. F. Sodium and Sodium-Ion Energy Storage Batteries. *Curr. Opin. Solid State Mater. Sci.* **2012**, *16*, 168−177.

(3) Delmas, C.; Fouassier, C.; Hagenmuller, P. Structural Classification and Properties of the Layered Oxides. *Physica B+C* **1980**, *99*, 81−85.

(4) Fouassier, C.; Delmas, C.; Hagenmuller, P. Evolution structurale et proprietes physiques des phases A_XMO_2 (A = Na, K; M = Cr, Mn, Co) ($x \leq 1$). *Mater. Res. Bull.* **1975**, *10*, 443−449.

(5) Ohzuku, T.; Iwakoshi, Y.; Sawai, K. Formation of Lithium-Graphite Intercalation Compounds in Nonaqueous Electrolytes and Their Application as a Negative Electrode for a Lithium Ion (Shuttlecock) Cell. *J. Electrochem. Soc.* **1993**, *140*, 2490.

(6) Xu, J.; Lee, D. H.; Meng, Y. S. Recent Advances in Sodium Intercalation Positive Electrode Materials for Sodium Ion Batteries. *Funct. Mater. Lett.* **2013**, *06*, 1330001.

(7) Yabuuchi, N.; Kajiyama, M.; Iwatate, J.; Nishikawa, H.; Hitomi, S.; Okuyama, R.; Usui, R.; Yamada, Y.; Komaba, S. P2-Type $Na_x[Fe_{1/2}Mn_{1/2}]O_2$ Made from Earth-Abundant Elements for Rechargeable Na Batteries. *Nat. Mater.* **2012**, *11*, 512−517.

(8) Xu, J.; Lee, D. H.; Clément, R. J.; Yu, X.; Leskes, M.; Pell, A. J.; Pintacuda, G.; Yang, X.; Grey, C. P.; Meng, Y. S. Identifying the Critical Role of Li Substitution in P2 − $Na_X[Li_YNi_ZMn_{1-Y-Z}]O_2$ ($0 < X, Y, Z < 1$) Intercalation Cathode Materials for High-Energy Na-Ion Batteries. *Chem. Mater.* **2014**, *26*, 1260−1269.

(9) Jache, B.; Adelhelm, P. Use of Graphite as a Highly Reversible Electrode with Superior Cycle Life for Sodium-Ion Batteries by Making Use of Co-Intercalation Phenomena. *Angew. Chem., Int. Ed.* **2014**, *53*, 10169−10173.

(10) Stevens, D. A.; Dahn, J. R. The Mechanisms of Lithium and Sodium Insertion in Carbon Materials. *J. Electrochem. Soc.* **2001**, *148*, A803.

(11) Chevrier, V. L.; Ceder, G. Challenges for Na-Ion Negative Electrodes. *J. Electrochem. Soc.* **2011**, *158*, A1011.

(12) Komaba, S.; Matsuura, Y.; Ishikawa, T.; Yabuuchi, N.; Murata, W.; Kuze, S. Redox Reaction of Sn-Polyacrylate Electrodes in Aprotic Na Cell. *Electrochem. Commun.* **2012**, *21*, 65−68.

(13) Ellis, L. D.; Hatchard, T. D.; Obrovac, M. N. Reversible Insertion of Sodium in Tin. *J. Electrochem. Soc.* **2012**, *159*, A1801−A1805.

(14) Wang, J. W.; Liu, X. H.; Mao, S. X.; Huang, J. Y. Microstructural Evolution of Tin Nanoparticles during In Situ Sodium Insertion and Extraction. *Nano Lett.* **2012**, *12*, 5897−5902.

DOI: 10.1021/acs.chemmater.5b01984
Chem. Mater. 2015, 27, 5633−5640

(15) Xiao, L.; Cao, Y.; Xiao, J.; Wang, W.; Kovarik, L.; Nie, Z.; Liu, J. High Capacity, Reversible Alloying Reactions in SnSb/C Nanocomposites for Na-Ion Battery Applications. *Chem. Commun.* **2012**, *48*, 3321.
(16) Liu, Y.; Xu, Y.; Zhu, Y.; Culver, J. N.; Lundgren, C. A.; Xu, K.; Wang, C. Tin-Coated Viral Nanoforests as Sodium-Ion Battery Anodes. *ACS Nano* **2013**, *7*, 3627−3634.
(17) Su, D.; Ahn, H.-J.; Wang, G. SnO_2@graphene Nanocomposites as Anode Materials for Na-Ion Batteries with Superior Electrochemical Performance. *Chem. Commun.* **2013**, *49*, 3131−3133.
(18) Su, D.; Xie, X.; Wang, G. Hierarchical Mesoporous SnO Microspheres as High Capacity Anode Materials for Sodium-Ion Batteries. *Chem. - Eur. J.* **2014**, *20*, 3192−3197.
(19) Wu, L.; Hu, X.; Qian, J.; Pei, F.; Wu, F.; Mao, R.; Ai, X.; Yang, H.; Cao, Y. A Sn−SnS−C Nanocomposite as Anode Host Materials for Na-Ion Batteries. *J. Mater. Chem. A* **2013**, *1*, 7181.
(20) Kim, Y. Y.; Kim, Y. Y.; Choi, A.; Woo, S.; Mok, D.; Choi, N. S.; Jung, Y. S.; Ryu, J. H.; Oh, S. M.; Lee, K. T. Tin Phosphide as a Promising Anode Material for Na-Ion Batteries. *Adv. Mater.* **2014**, *26*, 4139−4144.
(21) Qian, J.; Xiong, Y.; Cao, Y.; Ai, X.; Yang, H. Synergistic Na-Storage Reactions in Sn_4P_3 as a High-Capacity, Cycle-Stable Anode of Na-Ion Batteries. *Nano Lett.* **2014**, *14*, 1865−1869.
(22) Qu, B.; Ma, C.; Ji, G.; Xu, C.; Xu, J.; Meng, Y. S.; Wang, T.; Lee, J. Y. Layered SnS_2-Reduced Graphene Oxide Composite - A High-Capacity, High-Rate, and Long-Cycle Life Sodium-Ion Battery Anode Material. *Adv. Mater.* **2014**, *26*, 3854−3859.
(23) Hummers, W. S., Jr.; Offeman, R. E. Preparation of Graphitic Oxide. *J. Am. Chem. Soc.* **1958**, *80*, 1339.
(24) Ravel, B.; Newville, M. ATHENA, ARTEMIS, HEPHAESTUS: Data analysis for X-ray absorption spectroscopy using IFEFFIT. *J. Synchrotron Radiat.* **2005**, *12*, 537−541.
(25) Wu, Q.; Jiao, L.; Du, J.; Yang, J.; Guo, L.; Liu, Y.; Wang, Y.; Yuan, H. One-Pot Synthesis of Three-Dimensional SnS_2 Hierarchitectures as Anode Material for Lithium-Ion Batteries. *J. Power Sources* **2013**, *239*, 89−93.
(26) Patterson, A. L. The Scherrer Formula for X-Ray Particle Size Determination. *Phys. Rev.* **1939**, *56*, 978−982.
(27) Seo, J. W.; Jang, J. T.; Park, S. W.; Kim, C.; Park, B.; Cheon, J. Two-Dimensional SnS_2 Nanoplates with Extraordinary High Discharge Capacity for Lithium Ion Batteries. *Adv. Mater.* **2008**, *20*, 4269−4273.
(28) Baker, H.; Okamoto, H. *ASM Handbook*; ASM International: 1992.
(29) Hu, M.; Jiang, Y.; Sun, W.; Wang, H.; Jin, C.; Yan, M. Reversible Conversion-Alloying of Sb_2O_3 as a High-Capacity, High-Rate, and Durable Anode for Sodium Ion Batteries. *ACS Appl. Mater. Interfaces* **2014**, *6*, 19449−19455.
(30) Mansour, A. N.; Mukerjee, S.; Yang, X. Q.; McBreen, J. In Situ XAS of the Reaction Mechanism of Lithium with Tin-Based Composite Oxide Glass. *J. Synchrotron Radiat.* **1999**, *6*, 596−598.
(31) Baggetto, L.; Bridges, C. A.; Jumas, J.-C.; Mullins, D. R.; Carroll, K. J.; Meisner, R. A.; Crumlin, E. J.; Liu, X.; Yang, W.; Veith, G. M. The Local Atomic Structure and Chemical Bonding in Sodium Tin Phases. *J. Mater. Chem. A* **2014**, *2*, 18959−18973.
(32) Smith, A. J.; Meek, P. E.; Liang, W. Y. Raman Scattering Studies of SnS_2 and $SnSe_2$. *J. Phys. C: Solid State Phys.* **1977**, *10*, 1321−1333.
(33) Wang, C.; Tang, K.; Yang, Q.; Qian, Y. Raman Scattering, Far Infrared Spectrum and Photoluminescence of SnS_2 Nanocrystallites. *Chem. Phys. Lett.* **2002**, *357*, 371−375.
(34) Radovsky, G.; Popovitz-Biro, R.; Staiger, M.; Gartsman, K.; Thomsen, C.; Lorenz, T.; Seifert, G.; Tenne, R. Synthesis of Copious Amounts of SnS_2 and SnS_2/SnS Nanotubes with Ordered Superstructures. *Angew. Chem., Int. Ed.* **2011**, *50*, 12316−12320.
(35) Mei, L.; Xu, C.; Yang, T.; Ma, J.; Chen, L.; Li, Q.; Wang, T. Superior Electrochemical Performance of Ultrasmall SnS_2 Nanocrystals Decorated on Flexible RGO in Lithium-Ion Batteries. *J. Mater. Chem. A* **2013**, *1*, 8658.
(36) Luo, B.; Fang, Y.; Wang, B.; Zhou, J.; Song, H.; Zhi, L. Two dimensional graphene−SnS_2 hybrids with superior rate capability for lithium ion storage. *Energy Environ. Sci.* **2012**, *5*, 5226.
(37) Schwan, J.; Ulrich, S.; Batori, V.; Ehrhardt, H.; Silva, S. R. P. Raman Spectroscopy on Amorphous Carbon Films. *J. Appl. Phys.* **1996**, *80*, 440−447.
(38) Wang, G.; Wang, B.; Wang, X.; Park, J.; Dou, S.; Ahn, H.; Kim, K. Sn/graphene nanocomposite with 3D architecture for enhanced reversible lithium storage in lithium ion batteries. *J. Mater. Chem.* **2009**, *19*, 8378.

DOI: 10.1021/acs.chemmater.5b01984
Chem. Mater. 2015, 27, 5633−5640